Chin. J. Geochem. (2015) 34(1):1–12
DOI 10.1007/s11631-014-0029-z

Coupled alkali feldspar dissolution and secondary mineral precipitation in batch systems: 5. Results of K-feldspar hydrolysis experiments

Peng Lu · Hiromi Konishi · Eric Oelkers · Chen Zhu

Received: 23 December 2014 / Revised: 26 December 2014 / Accepted: 26 December 2014 / Published online: 11 January 2015

Abstract This paper explores how dissolution and precipitation reactions are coupled in batch reactor experimental systems at elevated temperatures. This is the fifth paper in our series of "Coupled Alkali Feldspar Dissolution and Secondary Mineral Precipitation in Batch Systems." In the previous four papers we presented batch experiments of alkali-feldspar hydrolysis and explored the coupling of dissolution and precipitation reactions (Fu et al. in Chem Geol 91:955–964, 2009; Zhu and Lu in Geochim Cosmochim Acta 73:3171–3200, 2009; Zhu et al.in Geochim Cosmochim Acta 74:3963–3983, 2010; Lu et al. in Appl Geochem 30:75–90, 2013). Here, we present the results of additional K-rich feldspar hydrolysis experiments at 150 °C. Our solution chemistry measurements have constrained feldspar dissolution rates, and our high resolution transmission electron microscopy work has identified boehmite precipitation. Reaction path modeling of K-feldspar dissolution and boehmite precipitation simulated the coupled reactions, but only with forced changes of boehmite rate law in the middle of experimental duration. The results which are reported in this article lend further support to our hypothesis that slow secondary mineral precipitation explains part of the well-known apparent discrepancy between lab measured and field estimated feldspar dissolution rates (Zhu et al. in Water–rock interaction, 2004).

Keywords Kinetics · Feldspar · Geochemical modeling · Rate law · Water-rock interaction

P. Lu · H. Konishi · C. Zhu (✉)
Department of Geological Sciences, Indiana University, Bloomington, IN 47408, USA
e-mail: chenzhu@indiana.edu

Present Address:
P. Lu
EXPEC Advance Research Center, Saudi Aramco Oil Company, Dhahran 31311, Saudi Arabia

Present Address:
H. Konishi
Department of Geology, Faculty of Science, Niigata University, Niigata 950-2181, Japan

E. Oelkers
Laboratoire de Geochimie, CNRS, 38 Rue Des Trente-Six Ponts, 31400 Toulouse, France

E. Oelkers
Earth Sciences, University College London, Gower Street, London WC1E 6B, UK

C. Zhu
Department of Earth Sciences, Zhejiang University, Hangzhou 300027, China

1 Introduction

The coupling of dissolution reaction and precipitation reactions may partly explain the well-known discrepancy (for the discrepancy, see Paces 1973; Siegel and Pfannkuch, 1984; Velbel 1990; Brantley 1992; Blum and Stillings 1995; Drever and Clow 1995; White and Brantley 2003; Zhu 2005) between laboratory measured and field estimated feldspar dissolution rates (Zhu et al. 2004; Zhu 2005; Zhu et al. 2006; Ganor et al. 2007; Hereford et al. 2007; Zhu 2009; Zhu et al. 2010; Lu et al. 2013). In fact, the overall dissolution rate of primary feldspar depends on the relative rates of all kinetically controlled reactions in a system (Lasaga 1998). Unlike in the laboratory, feldspar dissolution in natural systems occurs in the context of a reaction network which controls the individual heterogeneous reactions (Zhu 2009). Specifically, the slow precipitation of a secondary mineral result in

accumulation of solutes in the aqueous solution that makes the solution be close to the equilibrium with respect to the primary minerals (increased saturation state), and the diminishing thermodynamic drive near equilibrium result in much reduced rates as compared to the far from equilibrium rates (Zhu et al. 2004, 2010).

Numerous other hypotheses have also proposed to explain the apparent lab-field discrepancy (see Zhu 2005 for a review). Briefly, the preferential and stagnant flow paths prevalent in field systems lead to all field samples as mixed waters and field rates as a mixture of fast and slow rates (Li et al. 2008). Surface reactivity and reactive surface areas may also change significantly due to the opening and close of etch pits (Gautier et al. 2001; Beig and Lüttge 2006), secondary mineral coatings on the primary mineral surfaces (Nugent et al. 1998; Hellmann et al. 2003; Cubilas et al. 2005; Zhu et al. 2006), or formation of an amorphous layer (Daval et al. 2011).

To test our hypothesis, we have conducted a series of experiments of feldspar dissolution and secondary mineral precipitation in batch systems (Fu et al. 2009; Zhu and Lu 2009; Zhu et al. 2010; Lu et al. 2013). Since these reactions are too slow to be measured at ambient temperature and circumneutral pH conditions (Ganor et al. 2007), the experiments were conducted at 200 °C and at 300 bars. These experiments used perthitic feldspars, and dissolution of albite laminae dominated the experiments while K-rich feldspar laminae were supersaturated (Fu et al. 2009; Zhu and Lu 2009). In the present article we report additional experiments using K-rich feldspars. We also used high resolution transmission electron microscopy (HRTEM) to characterize the secondary minerals and to attempt to determine whether an amorphous layer has formed on feldspar surfaces. Numerical reaction path modeling simulated the feldspar hydrolysis experiments by matching modeling results with experimental data.

2 Methods

2.1 Starting materials

K-rich feldspar samples were obtained from Wards Scientific Establishments LLC and consisted of several 1–2 cm twinned crystals. The sample was ground with an agate mortar and pestle and then sieved to obtain the fraction between 50 and 100 μm. The resulting mineral powder was ultrasonically cleaned at least five times in methanol until the methanol was clear following cleaning (Lu et al. 2013). BET surface areas of each powder were measured using nitrogen and krypton prior to the experiments. The resulting surface areas are provided in Table 1. Surface areas were not measured following the experiments. The chemical compositions of these cleaned mineral samples as determined by electron microprobe are listed in Table 1 which yields the chemical formula of $K_{0.82}Na_{0.18}Al_{0.98}Si_{3.015}O_8$ which has been calculated following the method of Deer et al. (1992).

2.2 Dissolution experiments

Experiments were performed in a closed-system titanium rocking reactor with a volume of 400 cm^3 (Gautier et al. 1994; Harouiya and Oelkers 2004). The experiments were initiated by first placing the powdered feldspar into the reactor, followed by the fluid. The reactors were then sealed, placed in a furnace, rocking was initiated, and heated to 150 °C. Reactive fluid was sampled irregularly through a 0.1 micron filter. Sampling thus resulted in a change between fluid/feldspar ratios. The silica concentration of the outlet solution was determined via the molybdate blue method of Koroleff (1976). Aqueous Al concentrations were determined using a Perkin Elmer Zeeman 5,000 atomic adsorption spectrometer. Outlet solution pH was measured at 25 °C using a Metrohm© 744 pH meter coupled to a Metrohm© Pt1000/B/2 electrode with a 3 M KCl outer filling solution. The electrode was calibrated with NBS standards at pH 4.01, 6.86, and in acid standard solutions at pH 1.5 and 2.5 with an average error of less than 0.05 pH units.

Closed-system experiments were performed using the initial solutions comprised of MilliQ® demineralized H_2O and reagent grade KCl and HCl to obtain the solution compositions listed in Table 2. Two experiments were performed. Experiment R contained 251.76 g of aqueous solution R and 0.5017 g K-feldspar, and experiment L contains 252.47 g of aqueous solution L and 0.5058 g Alkali-feldspar. The experiment was stopped by cooling the reactors from 150 °C over the course of 18 h. The powder was separated from the reactive solution by filtration using a 0.45 micron cellouse-nitrate filter. The powder was dried overnight in an oven at 80 °C.

2.3 TEM characterization

Atomic scale HRTEM was used to characterize the reactants as well as the products (from reactor R). HRTEM and SAED measurements were done with both a Philips EM 420 and a CM300FEG microscope. Both microscopes operated at 120 and 295 kV, respectively.

Two sample preparation methods were used: ultrasonicate method and ultra-microtomy method. In the ultrasonicate method (Figs. 1, 2, 3), feldspar grains were hand-picked under a polarizing microscope. Selected crystals were then immersed in ethanol and ultrasonicated. A drop of the resulting suspension was placed onto lacey-carbon film supported by a standard Cu TEM grid and air-dried.

Ultra-microtomy was used to make cross sections of the surface of Au-coated K-feldspars. In the ultramicrotomy method (Figs. 4, 5, 6, 7, 8) feldspar grains were hand-picked under a polarizing microscope. We coated

Table 1 Chemical composition of the Alkali-feldspar used in this study

Sample and origin:	Alkali-feldspar (var. orthoclase), Colorado, United States
Composition (oxide percent)	
SiO_2	65.35
TiO_2	0
Al_2O_3	18.06
Fe_2O_3	0.03
MgO	0.00
CaO	0.01
SrO	0
BaO	0.01
Na_2O	2.03
K_2O	13.77
Rb_2O	0
Sum oxides	99.28
Initial BET surface area (cm^2/g)	955

Table 2 Initial solution compositions in the present study

Solution	HCl (mol/kg)	KCl (mol/kg)
Experiment R	1.027×10^{-4}	9.98×10^{-3}
Experiment L	2.011×10^{-4}	9.98×10^{-2}

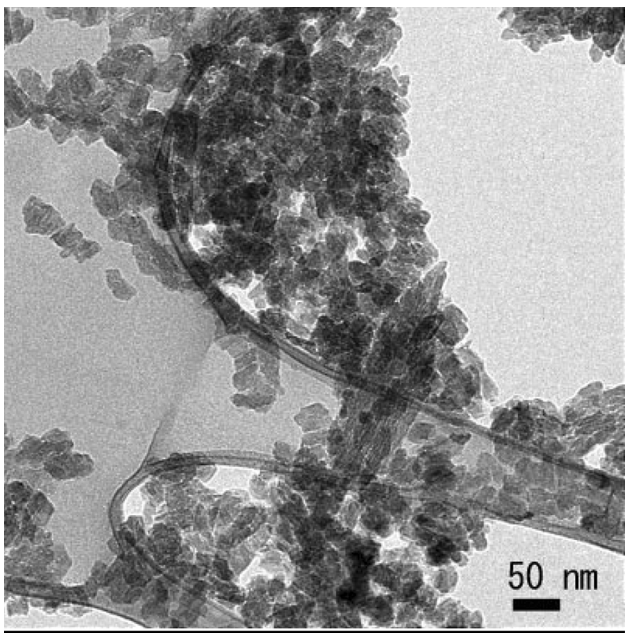

Fig. 1 Low magnification TEM image of boehmite aggregation. Boehmite crystals are 20–50 nm particles

Au on the K-feldspar grains to mark the crystal surface, embedded in BEEM capsules filled with epoxy resin (EPO-FIX), and aged the sample for 1 or 2 days at room temperature. If the resins were not hard enough after treatment, they were then put into an oven for several hours at 80 °C. The solidified samples (with resins) were cut by ultramicrotomy using a Sorvall MT2 microtome and a diamond knife. The resulting sections were collected on a Cu TEM grid or a holly carbon film supported on a Cu grid.

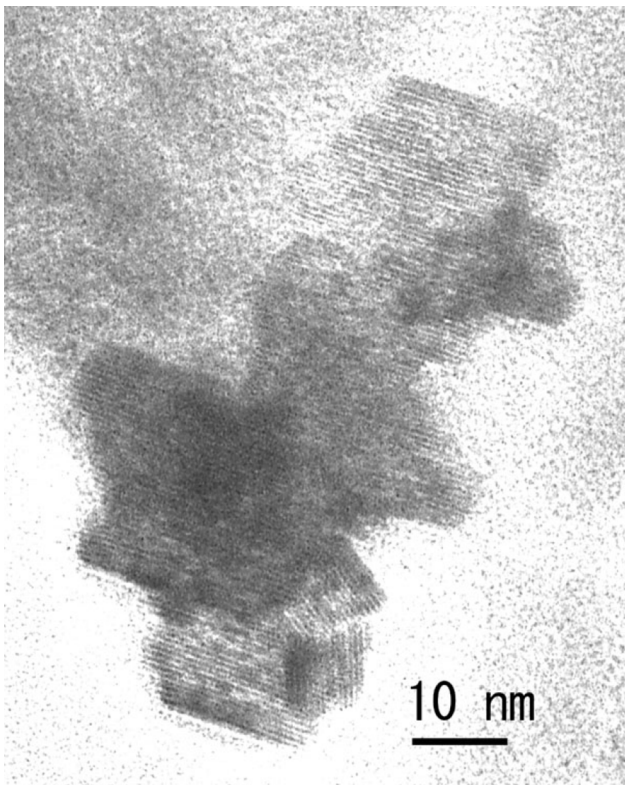

Fig. 2 HRTEM image of boehmite particles. Some grains have aligned to make a larger cluster. There are amorphous rims which surround the boehmite crystals, suggesting that they formed directly from aqueous solution. We can infer from this image and the fact that boehmite is loosely attached to the feldspar surface and are easily removed that there is no structural inheritance from feldspar to boehmite such that the boehmite is most likely formed via a dissolution-precipitation process, i.e. feldspar → aqueous components → boehmite

2.4 Standard state thermodynamic data

In all calculations the standard states for solids are defined as unit activity for pure end-member solids at the temperature and pressure of interest. The standard state for H_2O is the unit activity of pure water. For aqueous species other than H_2O, the standard state is the unit activity of the species in a hypothetical one molal solution referenced to infinite dilution at the temperature and pressure of interest. Equilibrium constants (log K) for reactions were calculated from the standard state thermodynamic properties for mineral end-members and aqueous species. The values of log K and the sources of thermodynamic properties that were used are listed in Table 4. In all cases, internally consistent

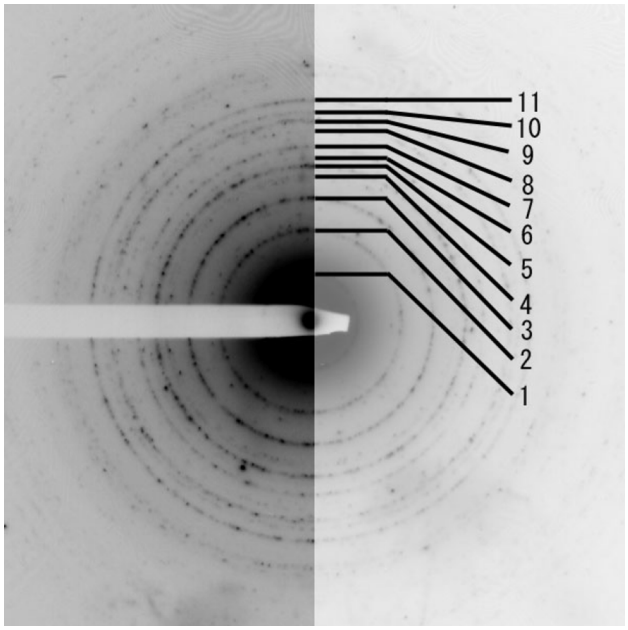

Fig. 3 ED from an aggregation of particles. Eleven reflections match the published data (JCPDS/ICDD file # 83-2384): *1* 020, *2* 120, *3* 031, *4* 131, *5* 051 and 200, *6* 220, *7* 151, *8* 080, *9* 231 and 002, *10* 022 and 171, *11* 251 and 122, indicate that the crystals in Fig. 2 are boehmite. The *dark spots* in the rings or between the rings are likely to be the contamination of feldspar fragments

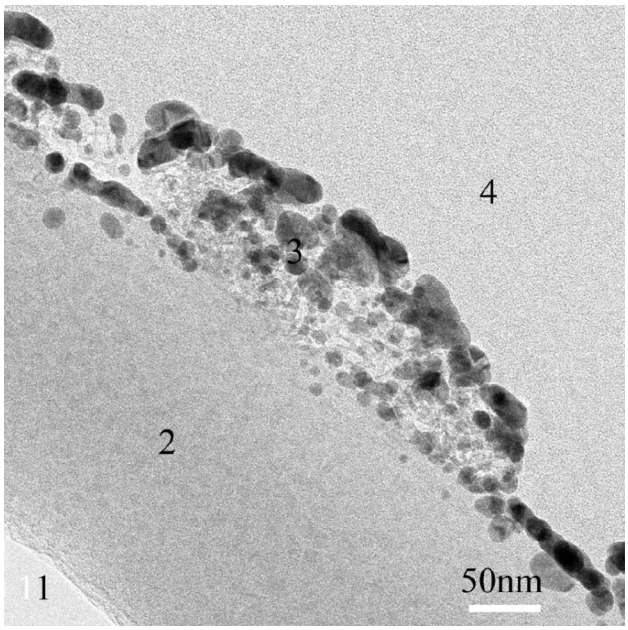

Fig. 4 TEM image of an ultramicrotomy sample (with *gold coating*) showing the spatial relationship between *gold coating* and K-feldspar crystal. *1* is a void, K-feldspar is labeled as *2,* Gold coating layer is labeled as *3, 4* is epoxy resin film

thermodynamic properties were used when possible. See Zhu and Lu (2009) for a detailed discussion of the choices regarding standard thermodynamic properties.

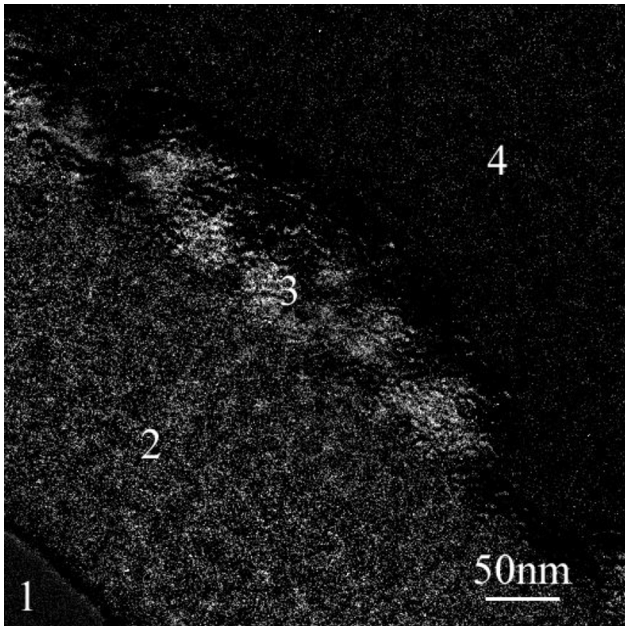

Fig. 5 EFTEM figure (Al map) of Fig. 4. Labels *1*, *2*, *3*, and *4* are the same as in Fig. 4. The layer 3 is Al concentrated *indicating* that secondary mineral product is more concentrated in Al than that in K-feldspar

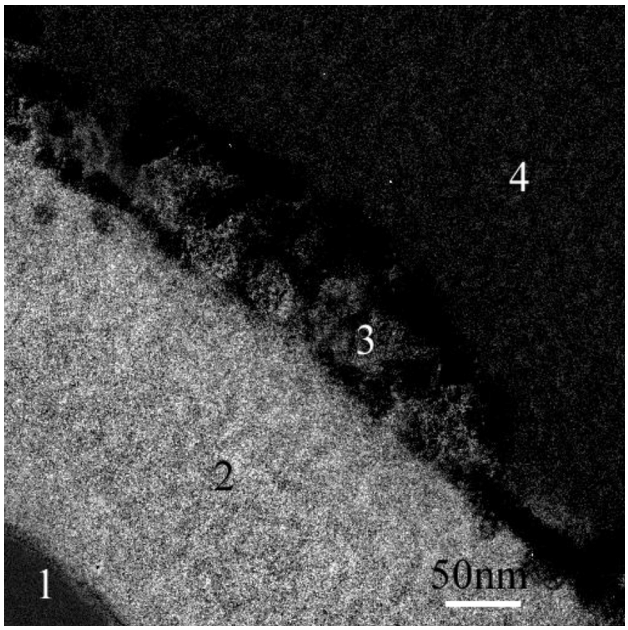

Fig. 6 EFTEM figure (Si map) of Fig. 4. Labels *1*, *2*, *3*, and *4* are the same as in Fig. 4. The layer 3 is Al concentrated but Si deficient, which *indicates* that K-feldspar forms an Al-rich, Si-deficient mineral (boehmite) after dissolution

3 Results and discussion

3.1 Solution chemistry

The evolution of fluid compositions during the experiments is listed as a function of time in Table 3. The

concentrations of Si in the fluid phase increased continuously with time. In experiment R, the Al concentrations increased gradually to 221 ppb at 792 h and decreased slightly to 192 ppb at the end of the experiment (1,152 h). In experiment L, the Al concentration increased gradually to 306 ppb at 792 h and decreased slightly to 192 ppb at the end of the reaction (1,152 h).

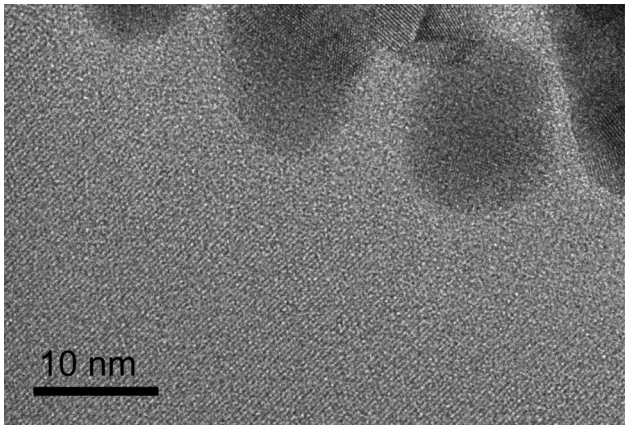

Fig. 7 HRTEM image of a cross section of the surface of K-feldspar. The amorphous materials have 5–10 nm width. They may be formed by electron beam damage. The *darker* contrast particles are gold

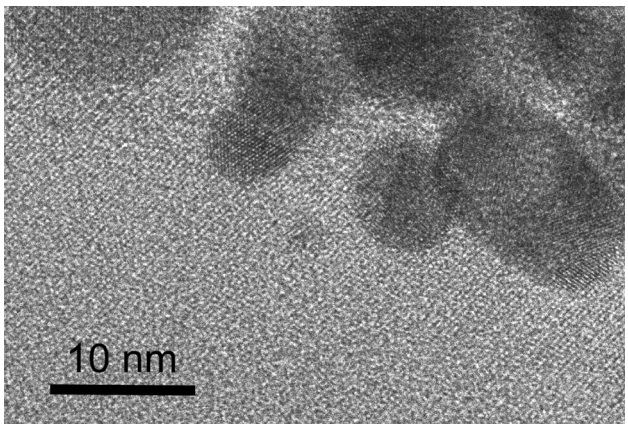

Fig. 8 HRTEM image of a cross section of the K-feldspar surface. The particles are gold, which are in direct contact with the lattice fringes of the K-feldspar

Numerous studies involving reaction kinetics of silicate minerals have shown that pH plays a particularly important role in the rate of mineral dissolution/precipitation processes (Oelkers et al. 1994; Oelkers 2001). Fluid pH in the present study was measured at ambient conditions (25 °C, 1 bar) and then re-calculated to experimental conditions (150 °C, P_{sat}) by taking an explicit account of the effect of temperature and pressure on the distribution of aqueous species. Accordingly, pH (*in situ*) was calculated for each sample taken during each experiment (Table 3). For the experiment R, aqueous solution pH increased from 4.05 to 4.79 during the first 10 days and then remained close to stable during 10–48 days. For experiment L, the aqueous solution pH increased from 3.79 to 5.32 during the first 10 days, and further increased slightly to 5.71 during days 10–48 Table 4.

3.2 TEM results

Secondary mineral products were identified as boehmite (Figs. 1, 2, 3). Boehmite occurs as an aggregation of single crystals ranging from 20 to 50 nm in size. Boehmite particles stick loosely onto the surface of feldspar and are easily taken off, suggesting both that there is no structural inheritance from feldspar to boehmite and that boehmite is most likely formed form a dissolution-precipitation process, i.e. feldspar → aqueous components → boehmite. All the ring patterns from an aggregation of the products match the published data of boehmite (JCPDS-ICDD: 83-2384) except for some spots which came from feldspar fragments or Fe oxides (Fig. 3). We detected Si from an aggregation of boehmite crystals, but the Si/Al ratio in the EDX spectrum is very small, unlike in the published data

Table 3 Measured concentrations of aqueous Al and Si as a function of time

Elapsed time (h)	PH (25°)	Total Si (ppm)	Total Al (ppb)	Sample size (gm)	pH (150°)
Experiment R					
0	4.04	0	0	–	4.052
240	5.40	6.87	138	7.29	4.793
552	5.44	8.14	202	6.97	4.692
792	5.52	8.68	221	9.75	4.689
1,152	5.54	9.30	192	–	4.740
Experiment L					
0	3.77	0	0	–	3.793
240	6.38	5.74	274	8.22	5.318
552	6.71	6.98	306	6.99	5.656
792	6.77	8.05	292	8.45	5.704
1,152	6.76	8.90	256	–	5.710

Table 4 Equilibrium constants used in this study

	25 °C 1 bar	150 °C	Ref.
Aqueous reactions			
$H_2O = OH^- + H^+$	−13.995	−11.631	(1)
$Al^{3+} + H_2O = Al(OH)^{2+} + H^+$	−4.964	−2.129	(2)
$Al^{3+} + 2H_2O = Al(OH)_2^+ + 2H^+$	−10.921	−5.045	(2)
$Al^{3+} + 3H_2O = Al(OH)_3^o + 3H^+$	−17.044	−9.168	(2)
$Al^{3+} + 4H_2O = Al(OH)_4^- + 4H^+$	−22.851	−13.747	(2)
$Al^{3+} + Na^+ + 4H_2O = NaAl(OH)_4^o + 4H^+$	−22.90	−13.097	(2)
$Al^{3+} + SiO_2^o + 2H_2O = AlH_3SiO4^{2+} + H^+$	−2.357	0.968	(2)
$Na^+ + H_2O = NaOH^o + H^+$	−14.205	−11.642	(3)
$SiO_2^o + H_2O = HSiO_3^- + H^+$	−9.585	−8.860	(3)
$SiO_2^o + Na^+ + H_2O = NaHSiO_3^o + H^+$	−7.754	−7.811	(3)
$K^+ + H_2O = KOH^o + H^+$	−14.439	−11.551	(3)
$H^+ + Cl^- = HCl^o$	−0.710	−0.518	(4)
$K^+ + Cl^- = KCl^o$	−2.535	0.308	(5)
$Na^+ + Cl^- = NaCl^o$	−0.777	−0.214	(3)
Minerals dissolution and precipitation			
$NaAlSi_3O_8$ (Albite) + $4H^+ = Al^{3+} + Na^+ + 3SiO_2^o + 2H_2O$	2.065	−1.539	(6)
AlO_2H (Boehmite) + $3H^+ = Al^{3+} + 2H_2O$	7.610	1.660	(7)
$Al_2Si_2O_5(OH)_4$ (Kaolinite) + $6H^+ = 2Al^{3+} + 2SiO_2^o + 5H_2O$	4.501	−3.419	(6)
$KAlSi_3O_8$ (Microcline) + $4H^+ = Al^{3+} + K^+ + 3SiO_2^o + 2H_2O$	−1.05	−3.260	(6)
$K_{0.82}Na_{0.18}Al_{0.98}Si_{3.015}O_8 + 1.95H_2O + 0.02H^+ = 0.82\ K^+ + 0.18Na^+ + 0.98Al(OH)_4^- + 3.015SiO_{2(aq)}$		−2.353	(8)
$KAl_3Si_3O_{10}(OH)_2$ (Muscovite) + $10H^+ = K^+ + 3Al^{3+} + 3SiO_2^o + 6H_2O$	11.22	−2.076	(6)
$NaAl_3Si_3O_{10}(OH)_2$ (Paragonite) + $10H^+ = Na^+ + 3Al^{3+} + 3SiO_2^o + 6H_2O$	14.397	−0.154	(6)
$Al_2Si_4O_{10}(OH)_2$ (Pyrophyllite) + $6H^+ = 2Al^{3+} + 4H_2O + 4SiO_2^o$	−1.724	−8.002	(6)
SiO_2 (Quartz) = SiO_2^o	−4.047	−2.694	(6)

(1) Haar et al. (1984), (2) Tagirov and Schott (2001), (3) Sverjensky et al. (1997), (4) McCollom and Shock (1997), (5) (Ho et al., 2000), (6) Holland and Powell (1998) for minerals and (1), (2), and (3) for aqueous species, (7) Hemingway et al. (1991), (8) Gautier et al. (1994)

on modified boehmite (Fig. 2 in Murakami et al. (1998)). The Si peak we found might be a contamination or come from a Si(Li) detector.

No thick amorphous layers, such as suggested as Heinemann et al. (2003) were observed on the surface of the Alkali-feldspar crystal. There is a light, bright area in the gold coating layer (layer 3 of Fig. 4) which is Al-rich (Figs. 5, 6). This indicates that an Al-rich mineral (probably boehmite) formed in response to feldspar dissolution. In some high-resolution images (e.g., Fig. 7), a thin amorphous layer is visible which likely formed by beam damage. In other cases (e.g., Fig. 8), lattice fringe of K-feldspar connects with gold particle directly and no amorphous layer is detected.

3.3 Geochemical modeling

The following assumptions were made to facilitate the modeling: (1) The amount of K-feldspar dissolution was calculated from Si release data, assuming that no secondary mineral consumes Si and K-feldspar dissolution is the only reaction that releases Si; (2) aqueous Na and K concentrations were derived from only K-feldspar dissolution; and (3) boehmite was the only secondary mineral to form. The amount of boehmite precipitated was calculated by subtracting measured Al concentrations from the total released Al due to K-feldspar dissolution, assuming stoichiometric primary phase dissolution. We plotted these predictions as open symbols in the figures to distinguish them from measured data, which is represented by solid symbols. The calculation of the equilibrium constants of K-feldspar ($K_{0.82}Na_{0.16}Al_{0.98}Si_{3.15}O_8$) at 150 °C, P_{sat} from its end members is problematic because of both solid solution and Si–Al ordering. We used experimental measured data to circumvent this. Gautier et al. (1994) obtained effective equilibrium constant for K-rich feldspar ($K_{0.81}Na_{0.15}Ba_{0.03}Al_{1.05}Si_{2.96}O_8$) dissolution reaction by regressing closed-system experimental data obtained in their study ($\log Ksp = -16.1$). We adopted this value considering the similar source of starting material.

The saturation states of selected minerals during the experiments were determined by speciation-solubility

Table 5 Saturation Indices calculations for minerals of interest

Elapsed time (hours)	Boehmite	Albite	Kaolinite	Microcline	K-feldspar	Muscovite	Paragonite	Quartz
Experiment R								
0	−0.95	−17.76	−7.04	−11.87	−13.77	−11.63	−17.71	−3.31
240	1.72	−5.27	3.08	−1.29	−2.87	4.29	0.11	−0.92
552	1.93	−4.86	3.65	−0.96	−2.53	5.05	0.94	−0.84
792	1.97	−4.71	3.78	−0.84	−2.40	5.25	1.17	−0.82
1,152	1.89	−4.63	3.68	−0.78	−2.34	5.14	1.09	−0.79
Experiment L								
0	−1.22	−18.35	−7.68	−11.66	−13.56	−11.96	−18.86	−3.30
240	1.58	−6.01	2.54	−0.41	−2.13	4.89	−0.92	−0.99
552	1.32	−5.59	2.19	−0.07	−1.78	4.71	−1.02	−0.90
792	1.26	−5.36	2.18	0.10	−1.60	4.74	−0.92	−0.84
1,152	1.19	−5.25	2.14	0.17	−1.51	4.69	−0.93	−0.80

calculation using PHREEQC (Table 5). The calculated saturation indices (SI) indicate that throughout the experiments the aqueous solution is under-saturated with respect to K-feldspar while supersaturated with respect to boehmite during the entire experiment R (see Fig. 10).

The following empirical rate equation (Burch et al. 1993) was used to model the reaction path of K-feldspar dissolution:

$$r / S = k_1[1 - \exp(-n_1 g)^{m_1}] + k_2[1 = \exp(-g)]^{m_2}, \quad (1)$$

where r and S stand for the rate of dissolution and reactive surface area of feldspar respectively. k_1 and k_2 denote the rate constants in units of mol s^{-1} m^{-2}, $g \equiv |\Delta G_r|/RT$, and n_1, m_1, and m_2 are empirical parameters fitted from experimental data. G_r stands for Gibbs free energy of the reaction of interest, R gas constant, and T the temperature in Kevin.

Literature parameters were used whenever possible to minimize the number of fitting parameters. k_1 was obtained from a far-from-equilibrium rate of 10^{-12} mol/m^2/s at 25 °C (pH 4) with an activation energy E_a of 51.7 kJ/mol (Blum and Stillings 1995). The k_1/k_2 ratio in Eq. (1), of 56.65 was taken from Hellmann and Tisserand (2006). Adopted values of n_1, m_1, and m_2 were 2×10^{-6}, 6, and 1.17, respectively, which are similar to those of Zhu et al. (2010) for modeling albite dissolution (5×10^{-6}, 6, and 1.17). Only a small percentage of K-feldspar was dissolved in the experiment (from 7.24×10^{-3} to 7.09×10^{-3} mol/kgw) so that we assumed the reactive surface areas of K-feldspar remained constant during the experiments. The measured BET surface area of 0.0955 m^2/g was used for the reactive surface area. The parameters used in this simulation are listed in Table 6.

For boehmite precipitation, we followed Bénézeth et al. (2008) and used the rate law,

$$r_{Bhm} = -k^*_{Bhm}(H^+)^{1.7}(e^{\frac{\Delta G_r}{RT}} - 1), \quad (2)$$

Table 6 Parameters and rate laws used in the simulation

Parameters/rate laws	Values
K-feldspar dissolution rate law	Eq. 1; Burch et al. (1993)
K-feldspar surface area	0.0955 m^2 g (constant)
m_1	2×10^{-6}
m_2	6
n	1.17
k_1	5×10^{-10} mol/m^2/s
k_1/k_2	56.65
Boehmite precipitation rate law (≤300 h)	Eq. 2; Bénézeth et al. (2008)
k_1^*	2×10^{-5} mol/kgw/s
Boehmite precipitation rate law (>300 h)	Eq. 4; TST
k_2^*	8×10^{-14} mol/kgw/s

where (H^+) stands for hydrogen ion activity. Bénézeth et al. (2008) conducted boehmite precipitation experiments for pH 6–9 at 100.3 °C . They found that the transition state theory (TST) $f(\Delta G_r)$ function fit to their data and the precipitation rate is a function of pH. Boehmite precipitation in our experiments occurred in the pH range of 4.05–4.74, at slightly more acidic conditions than those of Bénézeth et al. (2008). Nagy (1995) documented V-shaped pH dependence of aluminum oxyhydroxides dissolution rates and proposed an variation of rates on pH proportional to (H^+) at acidic conditions which we adopted. In the reaction path model the only fitted term in Eq. (2) was the effective rate constant k^*_{Bhm}, which was assumed to be constant here because the reactive surface areas for boehmite could not be assessed independently.

This geochemical model matched closely with the aqueous solution chemistry evolution during the first 300 h of the experiments (Fig. 9). Si concentrations increased

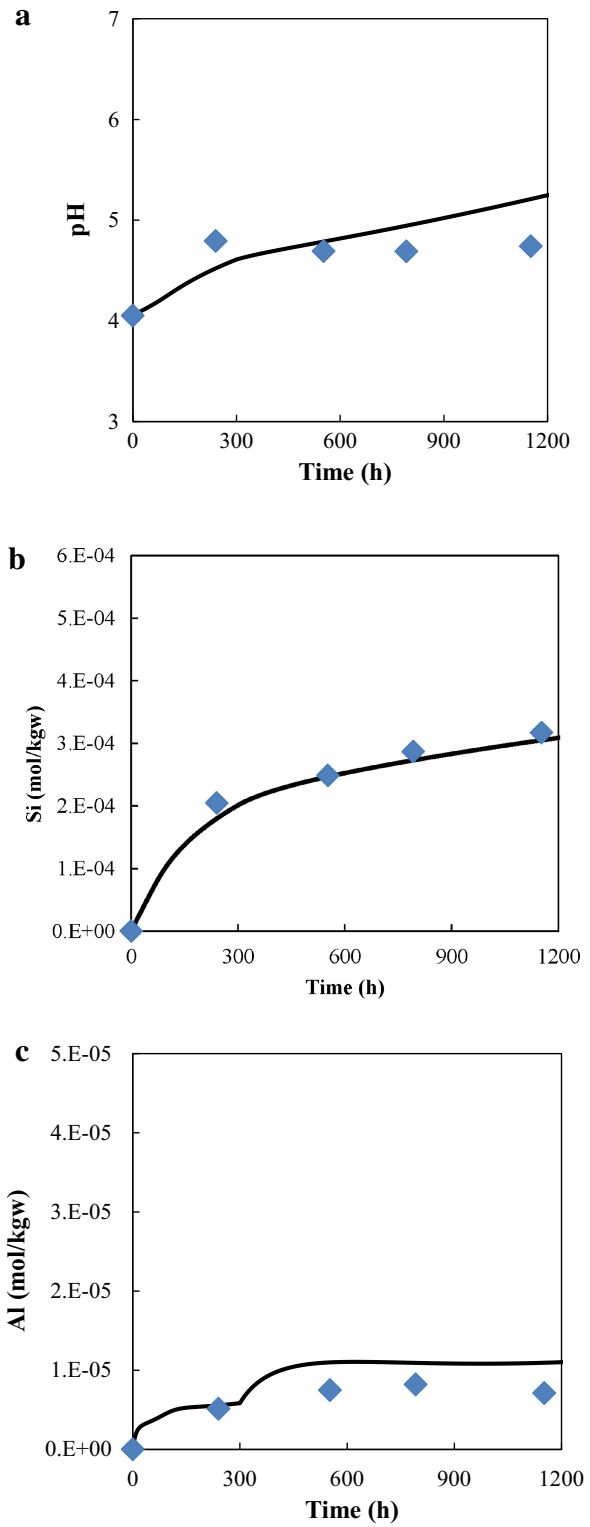

Fig. 9 Comparison of predicted solution chemistry from the reaction path model (*lines*) with experimental data (*symbols*) during the course of K-feldspar dissolution batch experiment R at 150 °C and Psat

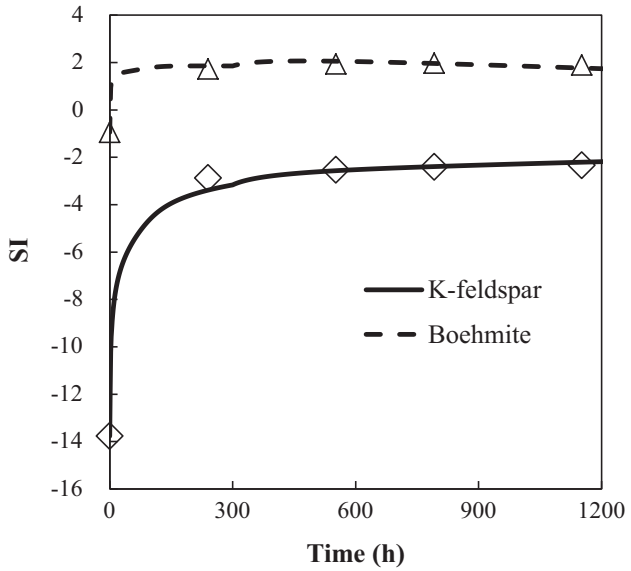

Fig. 10 Calculated change in K-feldspar and boehmite SI an evolution when compared with data from solubility calculations in experiment R

rapidly (0–300 h) as K-feldspar dissolved first starting from far from equilibrium, but this increase decelerated due to the $f(\Delta G_r)$ term in the rate law. The Al concentrations appear to reach a quasi-steady state as a result of the competition between K-feldspar dissolution and boehmite precipitation. The aqueous solution pH increased because both K-feldspar dissolution and boehmite precipitation consume H^+. Note that the dominant Al species is $Al(OH)_4^-$ during the experiments (Zhu 2009). The predicted SI over time matched well with speciation–solubility calculations for both primary mineral (K-feldspar) and secondary mineral (boehmite) (see Fig. 10).

The K-feldspar dissolution and boehmite precipitation reactions are closely coupled, which is consistent with the conclusions in Zhu et al. (2010). The ratios of K-feldspar dissolution and boehmite precipitation rates are close to unity on a mol s^{-1} kgw^{-1} basis although the individual rates decreased rapidly as solutes accumulate in the solution (Fig. 11a). The stoichiometric rate ratio is 1:1, reflecting the overall reaction,

$$K_{0.82}Na_{0.18}Al_{0.98}Si_{3.015}O_8 + H^+ \rightarrow 0.82K^+ + 0.18Na^+ + 0.98\ AlO(OH) + 3.015SiO_{2(aq)} + 0.01H_2O. \quad (3)$$

Two assumptions have been used in the modeling. The first is that a constant reactive surface area, though this is inconsistent with the experiments as no boehmite seeds were used in the experiments and boehmite reactive surface

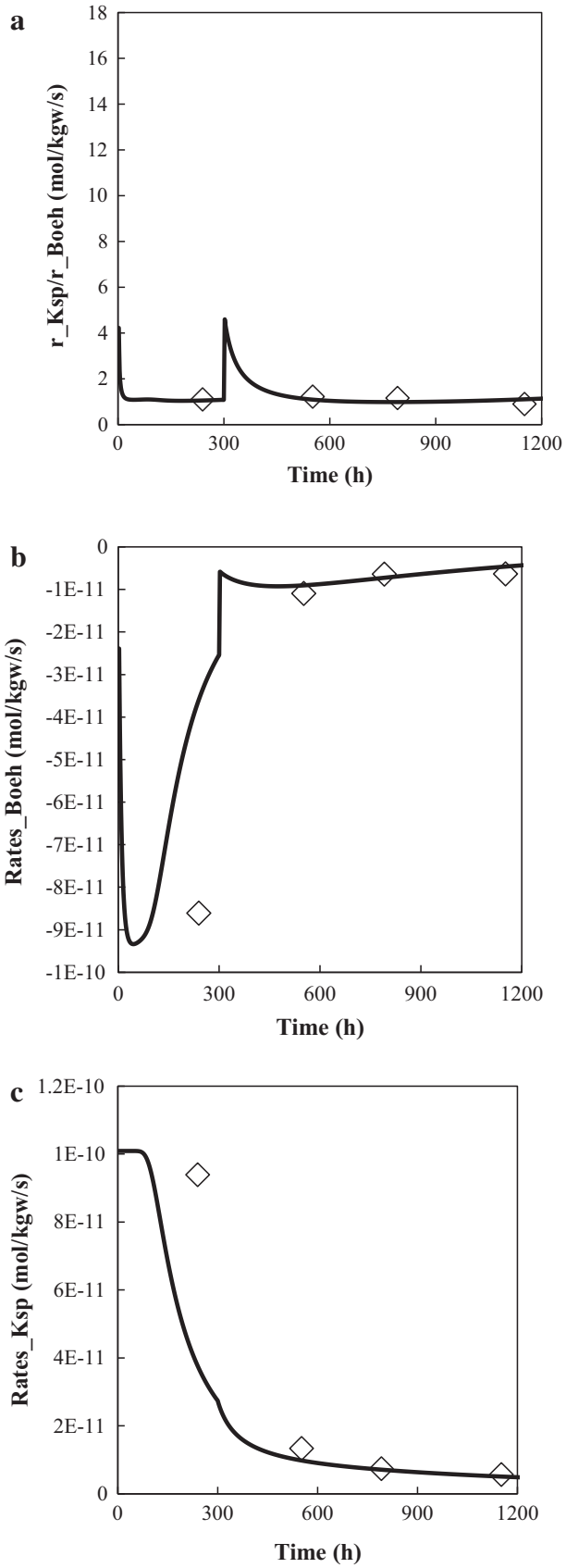

◀**Fig. 11** **a** Simulated ratios of K-feldspar dissolution rates versus boehmite precipitation rates when expressed in unit of mol s^{-1} kgw^{-1}. **b** Boehmite precipitation rates over time. **c** K-feldspar dissolution rates over time for experiment R. Bulk K-feldspar dissolution rates in unit of mol kgw^{-1} s^{-1} were estimated from stoichiometric release rates of Si and boehmite precipitation rates from the mass balance on Al. *Symbols* are rates derived from experimental data and *lines* are reaction path modeling results

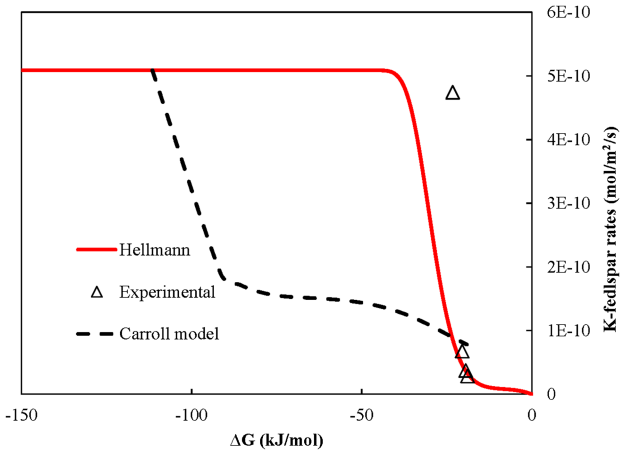

Fig. 12 Rates of K-feldspar dissolution normalized to the initial BET surface areas (in mol m^{-2} s^{-1}) for the experiment in experiment R. Symbols denote measured rates. The *red solid line* and *black dashed line indicate* calculations with rate law used in this study (Eq. (1)) with customized parameters and the model by Carroll and Knauss (2005). ΔG_r values were calculated from experimental data using PHREEQC

areas have certainly grown. The second assumption was that the K-feldspar dissolution rate is independent of pH, which was not a large factor because the range of pH change is relatively small (4.05–4.74).

For the modeling after 300 h, however, Al concentration and r_{Kfs}/r_{Bhm} ratios would not have matched between experimental data and model predictions if we continued to apply the boehmite precipitation expression of Eq. 2. Instead, predictions roughly matched with experimental data after 300 h with a rate law expression based on the TST (Lasaga 1981b; a; Aagaard and Helgeson 1982),

$$f(\Delta G_r) = \left(1 - \exp\left(\frac{\Delta G_r}{RT}\right)\right), \quad (4)$$

and an effective rate constant of 8×10^{-14} mol/kgw/s. Note that the sudden changes in the modeling results of Al concentrations, SI, r_{Kfs}/r_{Bhm}, r_{Bhm} and r_{Kfs} at 300 h (Figs. 9, 10, and 11) are due to the change of boehmite precipitation rate law after 300 h.

Other forms of the rate law and its parameters have also been tested. Oelkers et al. (1994) and Oelkers (2001) account for the inhibitory effects of dissolved aluminum on

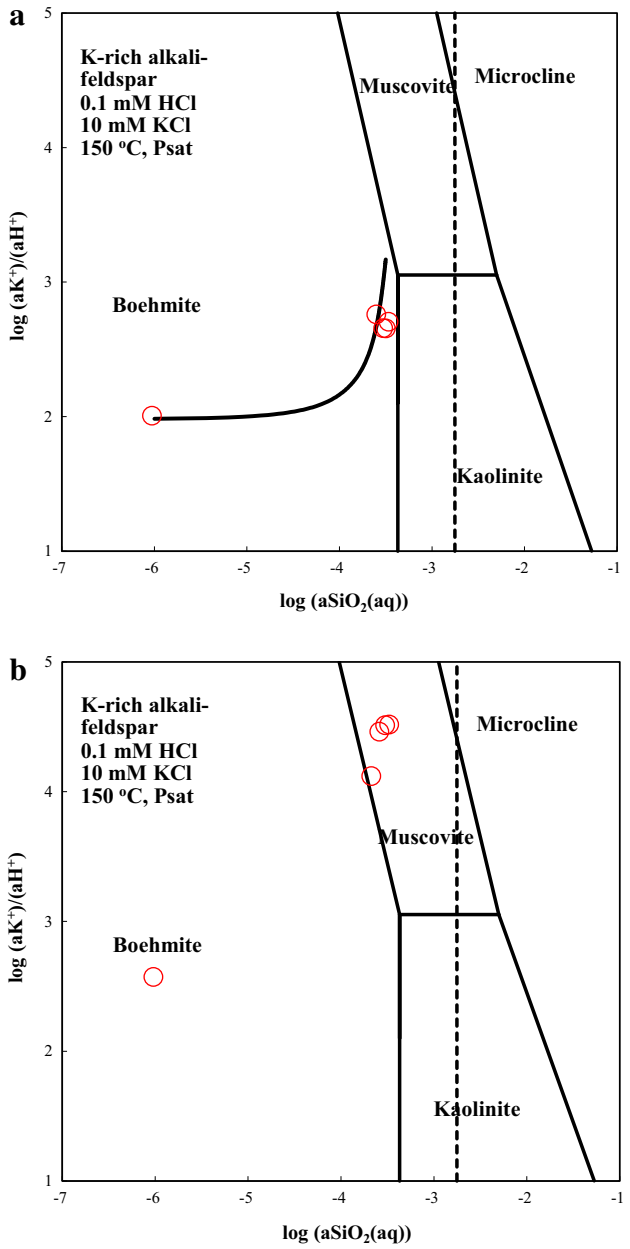

Fig. 13 Activity–activity diagram in the K_2O–Al_2O_3–SiO_2–H_2O–HCl system at 150 °C and Psat. The symbols represent values calculated from experimental data via speciation–solubility modeling. The *dashed lines* represent quartz solubility. **a** For experiment R. The *line denotes* to reaction path modeling prediction. **b** For experiment L

feldspar dissolution rates. These effects have been shown in experiments involving labradorite (Carroll and Knauss 2005). Carroll and Knauss (2005) adopted the Oelkers' approach on Al, and we tested Carroll and Knauss' (2005) equations in place of Eq. (1) in reaction path simulations. The results are partly shown in Fig. 12. We have also tested other alternative rate laws. If we had used a BCF rate law for boehmite precipitation instead but kept all other parameters the same, the Al and pH data would not have matched.

While the batch experimental data did not define a unique reaction path model, it was at least narrowed down to a limited set of plausible models. The reaction path of K-feldspar hydrolysis at 150 °C, P_{sat} was traced in the activity–activity diagram of K_2O–Al_2O_3–SiO_2–H_2O–HCl system (Fig. 13). The reaction proceeded within the boehmite field for the entire experiment duration which is consistent with the observation that boehmite is the most important secondary phase. The reaction path exceeded the experimental points at the end because the model slightly over-predicted pH after 600 h.

We attempted to model experiment L with the same approach for experiment R (data not shown). However, the model failed to predict the evolution of fluid pH probably because we did not consider muscovite as a secondary phase. Muscovite precipitation may be involved in this experiment because it is evident that most of the points are in the muscovite stability field of activity–activity diagram (Fig. 13b). However, we have insufficient data to constrain three reactions if muscovite precipitation is considered. Note that we did not analyze Na or K concentrations.

Overall, the results here showed the importance of coupled reactions in regulating the reaction rates. The coupling "arrested" the system to a steady state that dissolution of the primary mineral proceeded at a near equilibrium region where the dissolution rates are greatly reduced as compared to the far from equilibrium rates. This regulation may explain part of the apparent field-lab discrepancy (Zhu et al. 2004).

3.4 Conclusions and remarks

This study presented a detailed analysis of coupled alkali-feldspar dissolution and secondary mineral precipitation at an elevated temperature. The modeling results of these experiments confirmed the conclusions that the K-feldspar dissolution and boehmite precipitation reactions are closely coupled and consistent with the conclusions in Zhu et al. (2010). The modeling results substantiated our hypothesis (Zhu et al. 2004) that slow secondary mineral precipitation controls the dissolution rates of the primary phases and partly explains part of the well-known apparent discrepancy between laboratory and field measured feldspar dissolution rates. However, our study also demonstrated the deficiency in our knowledge of the reactions. Even in these simple laboratory systems, we could not completely match the modeling results with experimental data. Therefore, the proliferation of coupled reactive transport models that involve dozens of heterogeneous reactions in sandstone

systems probably should be considered only as educated guesses due to their enormous uncertainties.

Acknowledgments A research grant from the State Key Laboratory of Ore Deposits at the Institute of Geochemistry, Chinese Academy of Sciences.

References

Aagaard P, Helgeson HC (1982) Thermodynamic and kinetic constraints on reaction rates among minerals and aqueous solutions. I. Theoretical considerations. Am J Sci 282:237–285

Beig MS, Lüttge A (2006) Albite dissolution kinetics as a function of distance from equilibrium: implications for natural feldspar weathering. Geochim Cosmochim Acta 70:1402–1420

Bénézeth P, Palmer DA, Wesolowski DJ (2008) Dissolution/precipitation kinetics of boehmite and gibbsite: application of a pH-relaxation technique to study near-equilirbium rates. Geochim Cosmochim Acta 72:2429–2453

Blum A, Stillings L (1995) Feldspar dissolution kinetics. In: Brantley SL, White AR (eds) Chemical weathering rates of silicate minerals. Mineralogical Society of America, Washington, pp 291–346

Brantley SL (1992) Kinetics of dissolution and precipitation-experimental and field results. In: Kharaka Y, Maest A (eds) Proceedings of the seventh international conference on water-rock interactions, Park City, Utah. Balkema, Rotterdam, pp 465–469

Burch TE, Nagy KL, Lasaga AC (1993) Free energy dependence of albite dissolution kinetics at 80 °C and pH 8.8. Chem Geol 105:137–162

Carroll SA, Knauss KG (2005) Dependence of labradorite dissolution kinetics on $CO_{2(aq)}$, $Al_{(aq)}$, and temperature. Chem Geol 217: 213–225

Cubilas P, Kohler S, Prieto M, Causserand C, Oelkers EH (2005) How do mineral coating affect dissolution rates? An experimental study of coupled $CaCO_3$ dissolution–$CaCO_3$ precipitation. Geochim Cosmochim Acta 69:5459–5476

Daval D, Sissmann O, Menguy N, Saldi GD, Guyot F, Martinez I, Corvisier J, Garcia B, Machouk I, Knauss KG, Hellmann R (2011) Influence of amorphous silica layer formation on the dissolution rate of olivine at 90° C and elevated pCO_2. Chem Geol 284:193–209

Deer W, Howie R, Zussman J (1992) An introduction to the rock forming minerals, 2nd edn. Longman Scientific and Technical Group, Inc, Oceanside

Drever JI, Clow DW (1995) Weathering rates in catchments. In: White AF, Brantley SL (eds) Chemical weathering rates of silicate minerals. Mineralogical Society of America, New York, pp 463–481

Fu Q, Lu P, Konishi H, Dilmore R, Xu H, Seyfried WE Jr, Zhu C (2009) Coupled alkali-feldspar dissolution and secondary mineral precipitation in batch systems: 1. New experiment data at 200 °C and 300 bars. Chem Geol 91:955–964

Ganor J, Lu P, Zheng Z, Zhu C (2007) Bridging the gap between laboratory measurements and field estimations of weathering using simple calculations. Environ Geol 53:599–610

Gautier J-M, Oelkers EH, Schott J (1994) Experimental study of K-feldspar dissolution rates as a function of chemical affinity at 150 °C and pH 9. Geochim Cosmochim Acta 58:4549–4560

Gautier JM, Oelkers EH, Schott J (2001) Are quartz dissolution rates proportional to BET surface areas? Geochim Cosmochim Acta 65:1059–1070

Haar L, Gallagher JS, Kell GS (1984) NBS/NRC steam tables: thermodynamic and transport properties and computer programs for vapor and liquid states of water in SI units. Hemisphere Publishing Corporation, New York 320p

Harouiya N, Oelkers EH (2004) An experimental study of the effect of aqueous fluoride on quartz and alkali-feldspar dissolution rates. Chem Geol 205:155–167

Heinemann S, Wirth R, Dresen G (2003) TEM study of a special grain boundary in a synthetic K-feldspar bicrystal: manebach Twin. Phys Chem Miner 30:125–130

Hellmann R, Penisson JM, Hervig RL, Thomassin JH, Abrioux MF (2003) An EFTEM/HRTEM high-resolution study of the near surface of labradorite feldspar altered at acid pH: evidence for interfacial dissolution-reprecipitation. Phys Chem Miner 30: 192–197

Hellmann R, Tisserand D (2006) Dissolution kinetics as a function of the Gibbs free energy of reaction: an experimental study based on albite feldspar. Geochim Cosmochim Acta 70:364–383

Hemingway BS, Robie RA, Apps JA (1991) Revised values for the thermodynamic properties of boehmite, AlO(OH), and related species and phases in the system Al-H-O. Am Mineral 76:445–457

Hereford AG, Keating E, Guthrie G, Zhu C (2007) Reactions and reaction rates in the aquifer beneath Pajarito Plateau, north-central New Mexico. Environ Geol 52:965–977

Ho PC, Bianchi H, Palmer DA, Wood RH (2000) Conductivity of dilute aqueous electrolyte solutions at high temperatures and pressures using a flow cell. J Solut Chem 29:217–235

Holland TJB, Powell R (1998) An internally consistent thermodynamic data set for phases of petrological interest. J Metamorph Geol 16:309–343

Koroleff F (1976) Determination of silicon. In: Grasshoff K (ed) Methods of seawater analysis. Spring Verlag, Newyork, pp 149–158

Lasaga AC (1981a) Rate laws of chemical reactions. In: Lasaga AC, Kirkpatrick RJ (eds) Kinetics of geochemical processes. Mineralogical Society of America, Washington, pp 1–68

Lasaga AC (1981b) Transition state theory. In: Lasaga AC, Kirkpatrick RJ (eds) Kinetics of geochemical processes. Mineralogical Society of America, Washington, pp 135–169

Lasaga AC (1998) Kinetic theory in the earth sciences. Princeton University Press, New York

Li L, Steefel CI, Yang L (2008) Scale dependence of mineral dissolution rates within single pores and fractures. Geochim Cosmochim Acta 72:360–377

Lu P, Fu Q, Seyfried WE Jr, Hedges SW, Soong Y, Jones K, Zhu C (2013) Coupled alkali feldspar dissolution and secondary mineral precipitation in batch systems: 2. New experiments with supercritical CO_2 and implications for carbon sequestration. Appl Geochem 30:75–90

McCollom TM, Shock EL (1997) Geochemical constraints on chemolithoautotrophic metabolism by microorganisms in seafloor hydrothermal systems. Geochim Cosmochim Acta 61:4375–4391

Murakami T, Kogure T, Kadohara H, Ohnuki T (1998) Formation of secondary minerals and its effects on anorthite dissolution. Am Mineral 83:1209–1219

Nagy KL (1995) Dissolution and precipitation kinetics of sheet silicates. In: White AF, Brantley SL (eds) Chemical weathering rates of silicate minerals. Mineralogical Society of America, Washington, pp 173–225

Nugent MA, Brantley SL, Pantano CG, Maurice PA (1998) The influence of natural mineral coatings on feldspar weathering. Nature 395:588–591

Oelkers EH (2001) General kinetic description of multioxide silicate mineral and glass dissolution. Geochim Cosmochim Acta 65:3703–3719

Oelkers EH, Schott J, Devidal JL (1994) The effect of aluminum, pH, and chemical affinity on the rates of aluminosilicate dissolution reactions. Geochim Cosmochim Acta 58:2011–2024

Paces T (1973) Steady-state kinetics and equilibrium between ground water and granitic rocks. Geochim Cosmochim Acta 37:2641–2663

Siegel DI, Pfannkuch HO (1984) Silicate dissolution influence on Filson Creek chemistry, northeastern Minnesota. Geol Soc Am Bull 95:1446–1453

Sverjensky DA, Shock EL, Helgeson HC (1997) Prediction of the thermodynamic properties of aqueous metal complexes to 5 Kb and 1000 °C. Geochim Cosmochim Acta 61:1359–1412

Tagirov B, Schott J (2001) Aluminum speciation in crustal fluids revisited. Geochim Cosmochim Acta 65:3965–3992

Velbel MA (1990) Influence of temperature and mineral surface characteristics on feldspar weathering rates in natural and artificial systems: a first approximation. Water Resour Res 26:3049–3053

White AF, Brantley SL (2003) The effect of time on the weathering of silicate minerals: why do weathering rates in the laboratory and field? Chem Geol 202:479–506

Zhu C (2005) In situ feldspar dissolution rates in an aquifer. Geochim Cosmochim Acta 69:1435–1453

Zhu C (2009) Geochemical modeling of reaction paths and geochemical reaction networks. In: Oelkers EH, Schott J (eds) Thermodynamics and kinetics of water-rock interaction. Mineralogical Society of America, Washington, pp 533–569

Zhu C, Blum AE, Veblen DR (2004) Feldspar dissolution rates and clay precipitation in the Navajo aquifer at Black Mesa, Arizona, USA. In: Wanty RB, Seal RRI (eds) Water-rock interaction. August Aimé Balkema, Saratoga Springs, pp 895–899

Zhu C, Lu P (2009) Alkali feldspar dissolution and secondary mineral precipitation in batch systems: 3. Saturation states of product minerals and reaction paths. Geochim Cosmochim Acta 73: 3171–3200

Zhu C, Lu P, Zheng Z, Ganor J (2010) Coupled alkali feldspar dissolution and secondary mineral precipitation in batch systems: 4. Numerical modeling of kinetic reaction paths. Geochim Cosmochim Acta 74:3963–3983

Zhu C, Veblen DR, Blum AE, Chipera SJ (2006) Naturally weathered feldspar surfaces in the Navajo Sandstone aquifer, Black Mesa, Arizona: electron microscopic characterization. Geochim Cosmochim Acta 70:4600–4616